8

Physics and Instrumentation in PET

Roberto Accorsi, Suleman Surti, and Joel S. Karp

The radioactive decay of many radioisotopes generates penetrating photons capable of escaping outside the matter in which the isotopes are located. From this radiation it is possible to image the spatial distribution of such isotopes inside an object. However, by itself the detection of a single photon outside the body of a patient carries minimal information on the location of its origin, unless some device capable of connecting the detection with the emission location is used. These devices are the optics of the imaging instrument and they identify, in combination with a position sensitive radiation detector, a line in space (the line of response, LOR) along which the photon must have originated (Fig. 8.1A,B). The LOR data are manipulated in reconstruction software to produce three-dimensional (3D) images of the activity distribution. When imaging humans, it is necessary to use photons capable of escaping undeflected from a few centimeters of tissue. The energy of these photons is such that their path cannot be bent by reflection (mirrors), refraction (lenses), or diffraction as in visible light optics. Nuclear scintigraphy and single photon emission computed tomography (SPECT) instrumentation resort to absorptive collimation, in which photons are selectively passed or absorbed depending on their emission location and angle of incidence on the optics. The drawback of this approach is that the wide majority of photons are lost before image reconstruction. For example, typical parallel-hole collimators [low energy—technetium-99m (^{99m}Tc; 140 keV); general purpose] pass on the order of 1 in 10,000 (10^{-4}) photons, but sensitivity is even lower for high-resolution and high-energy collimators, which need lower acceptance angles and thicker septa, respectively. Although sensitivity can be recouped by trading off resolution (as with high-sensitivity collimators) or field-of-view (as with converging collimators), it is the concept of absorptive collimation itself that implies an inefficient use of emitted photons.

For isotopes decaying by positron emission, an alternative approach is possible. Because two back-to-back photons are emitted, if both photons are detected, the LOR is immediately identified with no need of discarding any photons incident on the detector (Fig. 8.1C). Greatly

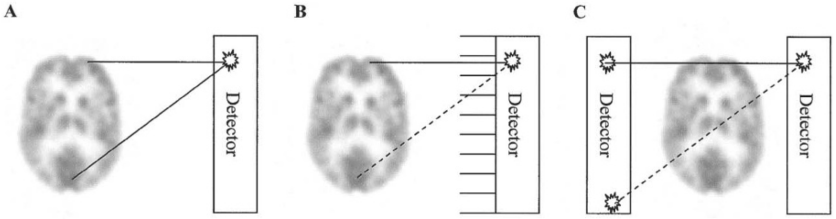

Figure 8.1. Pictorial representation of the identification of lines of response in nuclear imaging. A: Single photon imaging. With no collimation optics present it is impossible to establish the path of incoming photons. B: Single photon imaging. The presence of a collimator gives information on the path of incoming photons. In this case the detected photon must have come from the anterior part, rather than the posterior part, of the brain. Photons not parallel to the bores of the collimator are absorbed and thus lost. C: Positron emission tomography. When radioactive decay results in the emission of two colinear photons, it is possible to determine the path of the photons without a collimator. In principle, no incoming photons are lost.

increased sensitivity to incoming photons is one advantage of positron emission tomography (PET) over SPECT. Another is that most biologically significant elements (e.g., C, N, and O) have positron but no single photon emitting isotopes with practical half-lives. Radioisotope marking of biologically significant molecules is therefore usually more natural with PET rather than SPECT isotopes.

When compared to other techniques such as ultrasound, magnetic resonance imaging (MRI), and computed tomography (CT), PET is characterized, as is SPECT, by relatively poor spatial resolution but excellent sensitivity because the signal is generated by a number of atoms on the order of picomoles. Because the biodistribution of the radiotracer, rather than anatomic structures, is imaged in nuclear imaging, PET is most appropriate when functional information is sought.

Dedicated PET scanners have evolved in a number of different configurations over the years. Today, the most common design presents several rings of small scintillator crystals coupled to photomultiplier tubes (PMTs). In whole-body scanners, the ring diameter is about 80 to 90 cm. Together, all rings form a cylinder with a height limited by cost considerations to about 15 to 25 cm. These dimensions may be sensibly different in scanners designed for other, often specialized, purposes, such as brain, breast, and small animal imaging. Brain and animal scanners need a small transverse field of view and can be designed with a smaller radius to improve solid angle coverage, and thus increase sensitivity. If coincident events connecting many different rings are accepted, the scanner is said to operate in 3D mode. If only events originating in the plane of each ring (and, typically, a few adjacent rings) are collected, the scanner is said to operate in two-dimensional (2D) mode instead. In many 2D systems, septa are used to separate the rings and are retractable to allow both modes of operation on the same scanner.

The literature is rich with thorough presentations of PET (1,2). This chapter presents an essential summary of PET physics, instrumentation, and operation principles, with observations on the relevance of the concepts presented in pediatric applications. First, the physics at the basis of PET is discussed. Aspects influencing the performance of detection instrumentation are emphasized. The discussion of PET instrumentation starts from the parameters and the trade-offs involved in the choice of the scintillating material. Next, the different schemes that can be used to arrange the scintillating material in the scanner are presented. These schemes mainly concern how the light into which high-energy photons are converted in the scintillator is conveyed to the electronics. The data correction procedures necessary to achieve quantitatively accurate images are described next. Finally, the parameters used in the assessment of scanner performance and a brief overview of the choices available for image reconstruction are presented. Some considerations specific to the pediatric applications of PET close this chapter.

Radioactive Decay and Positron Emission

Radioactive decay of unstable isotopes usually occurs through three modalities: α, β, and γ. In its turn, β decay is subdivided in three different types: β^+, β^-, and electron capture (EC). β^+ decay follows the scheme

$$^{A}_{Z}X \rightarrow {}^{A}_{Z\text{-}1}\mathrm{Y} + \mathrm{e}^+ + \nu \tag{1}$$

where X and Y indicate the chemical species of the mother and daughter nuclei, respectively, Z is the atomic number (number of protons, which also identifies the chemical species) of the nucleus X, A its mass number (number of protons plus neutrons, which identifies the isotope within the species), e^+ is a positron, and ν a neutrino. The decay is governed by quantum mechanical laws (3) that select at random the kinetic energy E of the positron emerging from the decaying nucleus in the range from almost zero to a maximum possible value $E_{\max}$, which depends on the isotope ^{A}X. Table 8.1 shows values of $E_{\max}$ for sample PET isotopes.

As the radiotracer decays, the rate at which positrons are emitted declines over time. The activity A of the sample is defined as the average number of decays per unit over a short time interval. It varies with time according to the relationship

$$A(t) = A(t = 0)e^{-\lambda t} \tag{2}$$

where t is time and λ is the decay constant governing the rate of decay. It is the probability of decay of the isotope per unit time and is a physical constant for every isotope. λ is also connected to the half-life of the isotope, $\tau_{1/2}$, which is defined as the time it takes for the activity to halve, through the relationship

Table 8.1. Decay data for some positron emitters

Isotope	Half-life	Branching ratio of β^+ decay	$E_{\max}$ (MeV)	Production
^{11}C	20.4 min	>0.99	0.960	Cyclotron
^{13}N	9.97 min	>0.99	1.198	Cyclotron
^{15}O	122.2 s	>0.999	1.732	Cyclotron
^{18}F	110 min	0.97	0.633	Cyclotron
^{22}Na	2.6 y	0.90	0.545	Reactor
^{64}Cu	12.7 h	0.17	1.673	Cyclotron
^{68}Ga	67.6 m	0.89	2.921	Daughter of ^{68}Ge
^{82}Rb	1.27 m	0.95	3.379	Daughter of ^{82}Sr
^{124}I	4.17 d	0.23	1.535	Cyclotron

Source: Data from Chang J. Table of Nuclides, KAERI (Korea Atomic Energy Research Institute). Available at http://atom.kaeri.re.kr/ton/.

$$\tau_{1/2} = \frac{\ln 2}{\lambda} \tag{3}$$

as it can be worked out from Equation 2. The half-lives of isotopes of interest in nuclear medicine range from seconds to years. In SPECT, the most widely used isotope, ^{99m}Tc, has a half-life of about 6 hours. For PET, the half-life of fluorine 18 (^{18}F) is approximately 2 hours. This is about ideal because this is enough time to allow for isotope production, radiopharmaceutical synthesis, dose delivery, and imaging time while minimizing the dose burden to the patient, which also depends on $\tau_{1/2}$. The decay constant λ is related to the number N of nuclei present in the sample and the activity by the relationship

$$A = \lambda N. \tag{4}$$

It should be noted that Equation 2 governs the rate of decay of nuclei, which is not always the same as the rate of emission of positrons. In fact, different modes of decay may be available to a nucleus. For example, iodine 124 (^{124}I) undergoes β^+ decay only in 23% of the cases; in the remaining 77% the decay mode is EC, which does not produce any positrons. In such cases, it is important to account for this branching ratio when estimating the rate of positron emission from the decay rate of the nuclei. If the problem is to predict the decay over time of a certain type of activity measured at some other point in time, Equation 2 can be applied without worrying about the branching ratio, which is already accounted for in the measurement.

Interaction with Matter

Positron Annihilation

After decay, the positron leaves the site of emission and slows down in the surrounding material. As the positron is a relatively light, charged particle, it undergoes large-angle scattering interactions with other charged particles, which result in a tortuous path. The distance

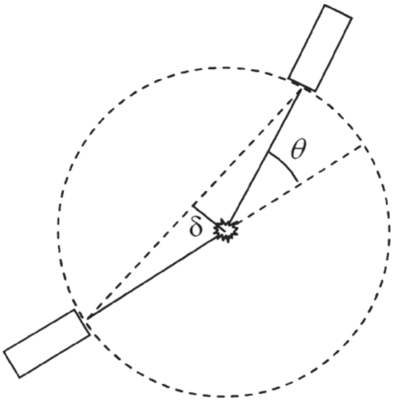

Figure 8.2. The small (~0.5-degree) deviation from 180 degrees in the emission of annihilation photons due to the residual momentum of the $e^- - e^+$ pair causes the corresponding line of response to be slightly misplaced (by the distance δ) from the annihilation site. This error is small, but it does limit the ultimate resolution of PET scanners. Compton scattering results in misplacement of events for the same basic reason, that is, because an angular deviation θ is introduced. In this case, misplacement is much more severe because θ is usually much greater than 0.5 degrees.

traveled from the nucleus, that is, the range of the particle, depends on the energy *E* with which the photon is emitted, the density of the surrounding material, as well as on the trajectory followed. The range is longer for positrons emitted with higher *E*. Maximum and average values of the range are found in the literature. For ^{18}F, carbon 11 (^{11}C), nitrogen 13 (^{13}N), and oxygen 15 (^{15}O) the average range is 0.6, 1.1, 1.5, and 2.5 mm, respectively.

During slowdown or once it has come to rest, the positron may combine with a surrounding electron and annihilate, that is, undergo a reaction in which positron and electron disappear and their total energy is converted into two or more photons. Fortunately, the great majority of annihilations results in the simultaneous emission of two (almost) back-to-back photons, each with an energy of 511 keV (4). The distance that each of the two annihilation photons must cover to reach the scanner depends on where the annihilation took place, so that the two photons can reach the scanner at slightly different times. However, this relative delay cannot be larger than a few nanoseconds (billionths of a second). The basic idea of PET is to attribute an event to an LOR every time that two photons are detected in approximate time coincidence.

Because the positron travels some distance from the nucleus before annihilation, annihilation photons are not generated at the site of the emitting nucleus, as happens for single photon emitters. Consequently, the nucleus can be located only approximately, the approximation worsening for increasing positron range. A second physical factor that intrinsically limits the spatial resolution of PET scanners is that annihilation photons are not emitted exactly along the same line (i.e., at a relative 180 degrees) in the laboratory frame of reference (5). This means that the annihilation site in general does not lie exactly on the line connecting the detection locations of the two photons (Fig. 8.2).

The ensuing positioning uncertainty δ is proportional to the diameter of the scanner (6) and reaches about 2 mm for a diameter of 90 cm. With current technology, this is one of the main factors limiting the resolution of whole-body PET scanners.

Gamma Attenuation, Scattering, and Random Coincidences

Annihilation photons may undergo interaction with surrounding materials before detection. Photons in the energy range relevant to PET interact with matter through two principal mechanisms: photoelectric absorption and Compton scattering. In photoelectric absorption, a photon is absorbed in an interaction with an atom in the surrounding material.

Effectively, the final result of a photoelectric event is that the photon disappears. Because in PET both annihilation photons need to be detected to form a valid event, photoelectric absorption of either photon outside the detector is sufficient to lose the annihilation event for image formation. Depending on the location and direction of the annihilation, the likelihood of attenuation changes, with higher losses for emission points lying deep within the patient. Therefore, attenuation must be compensated to obtain realistic images and quantitative data. Attenuation correction strategies for PET are described below and are based on the observation that, unlike in SPECT, in a collected event the total photon path crosses the object from side to side (Fig. 8.3). If a point source located anywhere along this line emits N_0 photons per unit time along the line, the rate at which events are recorded is

$$C = N_0\, e^{-\mu\rho D} \tag{5}$$

where μ is the mass attenuation coefficient of the material, which is known from its atomic composition and the energy of the photons, and ρ is its density. The key point is that the factor $e^{-\mu\rho D}$ can be obtained by direct measurement. In fact, if an external source of known activity A_0 is placed at one end of a given LOR, the count rate A measured at the other end of the LOR is given by

$$A = A_0\, e^{-\mu\rho D}. \tag{6}$$

Therefore, the factor $e^{-\mu\rho D}$ can be obtained experimentally from the ratio A/A_0 and then used to divide the coincident count rate C to recover the activity N_0. Note that this applies for sources anywhere along the LOR, that is, at any depth in the object.

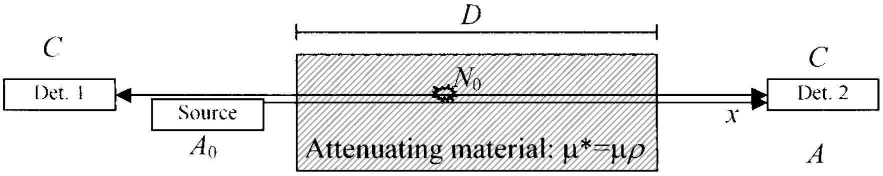

Figure 8.3. Attenuation correction in PET. The count rate recorded at detector 2 is C when exposed to annihilation photons in coincidence with detector 1 and A when exposed to the source of intensity A_0. The line connecting detector 2 to the source is separate from that connecting it to detector 1 only for illustration purposes.

For 511-keV photons in biologic materials, Compton scattering is much more likely to occur than photoelectric absorption. In Compton scattering, the photon loses some energy and its path is deviated by an angle θ (Fig. 8.2). The scattering angle is again selected in a random process governed by quantum mechanical laws (e.g., ref. 7). The energy of the scattered photon is related to θ by the Compton equation:

$$E'_\gamma = \frac{E_\gamma}{1 + \frac{E_\gamma}{m_e c^2}(1 - \cos\theta)} \tag{7}$$

where E_γ is the energy of the incident photon, m_e is the rest mass of the electron, and c is the speed of light. The product $m_e c^2$ is a physical constant and its value is 511 keV. The Compton equation shows that photons emerge from scattering with an energy that depends on the scattering angle. For example, for $\theta = 0$, or forward scattering, which is the limiting case in which the photon is not scattered at all, $E'_\gamma = 511$ keV; for $\theta = \pi$, which is the case of backscattering, that is, when the photon turns back, $E'_\gamma = 170$ keV. Unlike attenuation, scattering does not necessarily remove events from image reconstruction. Rather, it usually causes the incorrect association of a significant fraction of events to LORs, through the same basic mechanism of Figure 8.2, but in a much more dramatic way because of the much larger angular deviation involved. It is not at all uncommon that scatter events are assigned to LORs not even passing through the object, which does not happen for true events (i.e., unscattered events coming from the same annihilation) except for the much smaller effect of non-colinearity. Scatter events, in principle, could be rejected by measuring the energy of incoming photons and then accepting only those arriving with the correct energy, that is, 511 keV. As discussed below, existing equipment allows only an approximate measurement of the energy of photons, so that it is necessary to accept events with a measured energy of less than 511 keV to avoid discarding too many true events. Therefore, in practice, only photons whose measured energy is above a certain threshold (set at less than 511 keV) are accepted. This threshold is selected by setting the low-level discriminator (LLD) of the scanner. Because the Compton equation shows that E'_γ decreases as θ increases, increasing the LLD means confining θ closer to zero. From Figure 8.2, it is possible to see that this minimizes the error introduced. Whereas a high LLD setting does minimize the impact of scattering events, it has also other implications, as we shall see, and it cannot, alone, completely solve the problem of scatter contamination of the data; other methods, described below, are needed for full scatter compensation. The scattered photon can undergo further scattering, still governed by the same equations. Such events, as well as those in which both annihilation photons are scattered once, are referred to as multiple scattering.

Another type of spurious event, besides scattering events, can also enter the image. If more than one nucleus decays at approximately the same time, and for both events one of the two photons is lost, it is still possible that the two survivors are detected in coincidence. In this case a LOR is mistakenly associated to the unrelated photons (Fig. 8.4). This

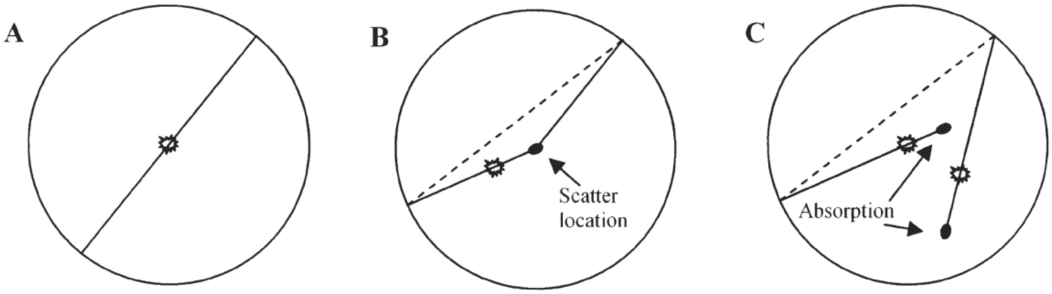

Figure 8.4. Pictorial representation of (A) a true coincidence, (B) a scatter event, and (C) a random coincidence. In B and C, the dashed line represents the line of response to which the event is assigned. It coincides with the path of the photons (solid line) only in case A.

type of event is called a random coincidence. The likelihood of random coincidences depends on the level and spatial distribution of activity and the temporal width of the coincidence window, as well as the geometry of the object. To appreciate this, it is helpful to consider that after the detection of a first photon above the LLD, the scanner waits up to a time τ for the photon emitted simultaneously to arrive. The time interval 2τ is called the time coincidence window. If the rate at which the first event is recoded is N events per unit time, then the rate at which random coincidences occur in the scanner is τN^2. Time coincidence windows are usually set between 6 and 12ns (billionths of a second, i.e., 10^{-9}s), depending on the scintillator.

PET Instrumentation

It is desirable to detect photons with high spatial, energy, and time resolution, with high sensitivity and count rate capabilities, all at reasonable cost. Different classes of detectors of high-energy photons have long been under development; no single class, however, offers the best performance in all respects. For example, solid-state detectors offer the best energy resolution, but their sensitivity is usually low, especially when their cost and availability over a large area are considered.

Commercial clinical PET cameras are based on scintillation detectors. In these systems, the photon interacts with a scintillating material, which converts the photon energy into visible or near-visible light. These low-energy photons are then conveyed to PMTs for conversion into an electrical signal. The front end of the PMT is the photocathode, which is a thin element of material capable of absorbing light photons and emitting electrons (called photoelectrons, because they are released by incident light) in proportion to the number of absorbed photons. Electrons are then multiplied by a cascade of electrodes (dynodes) to generate a measurable current and voltage, which is the output of the PMT. In summary, the role of the PMT is to convert the light emitted in the scintillator into an electric signal that is directly proportional to the intensity of the light signal. A much more compact alternative to PMTs are photodiodes. These are semiconductor devices capable of playing the same role. To date, their use has been hampered by their cost and instability with respect to fluctuations of temperature and applied voltage, and, often, the consequent need for cooling.

The electric signal generated by the PMT is then sent through pulse processing electronics that collect and process signals from the entire scanner. The part of this processing most typical of PET is the identification of events in time coincidence and their location on the detector for assignment to a LOR. Scanner designs differ mainly in the choice of the scintillator and the way light is conveyed (coupled) to PMTs.

Scintillating Material

Scintillators commonly considered for PET are listed in Table 8.2 along with some properties that characterize their performance. An ideal scintillator would have high sensitivity, that is, it would detect all incoming photons and record their energy and location of interaction accurately. Moreover, the timing properties of scintillators are also important because with fast scintillators a narrow time coincidence window can be used, which reduces the rate at which random coincidences are acquired as well as dead time effects (see below).

High sensitivity can be obtained with large volumes of scintillators. However, it is also important to be able to stop photons in a small volume to obtain precise positioning and thus high-resolution images. The thickness of a material necessary to absorb photons is regulated by the product $\mu^* = \mu\rho$ (e.g., see Equation 5). Materials with a high value of μ^* can stop photons within a relatively small distance and are preferred.

As already mentioned, an accurate energy measurement is important to differentiate scattering from true coincidence events. Figure 8.5 is a pictorial representation of the response of a real detector. This figure shows the number of incoming photons as a function of their measured energy. The peaks centered on 511 keV are due to 511-keV photons; because not all of these photons are exactly at 511 keV, it is evident that a real detector does not always measure energy accurately. This is due to a number of factors. An accurate measurement requires that, first, all the energy of the photon be deposited in the detector; second, that all deposited energy be transformed into light and converted into current with minimal fluctuations and losses; and, third, that all the current be collected and analyzed by pulse processing electronics.

Table 8.2. Properties of some scintillators used in PET

	NaI(Tl)	BGO	LSO	GSO	BaF_2	$LaBr_3$
Attenuation coefficient μ^* (cm^{-1})	0.34	0.95	0.87	0.7	0.45	0.47
Effective *Z*	50.6	74.2	65.5	58.6	52.2	46.9
Light output (photons/keV)	38	8	25	13	10	60
Light decay constant (ns)	230	300	40	60	0.6	25

BaF_2: Barium Fluoride; BGO: Bismuth Germanate; GSO: Gadolinium Oxyorthosilicate; $LaBr_3$: Lanthanum Bromide; LSO: Lutetium Oxyorthosilicate; NaI(Tl): Sodium Iodide.

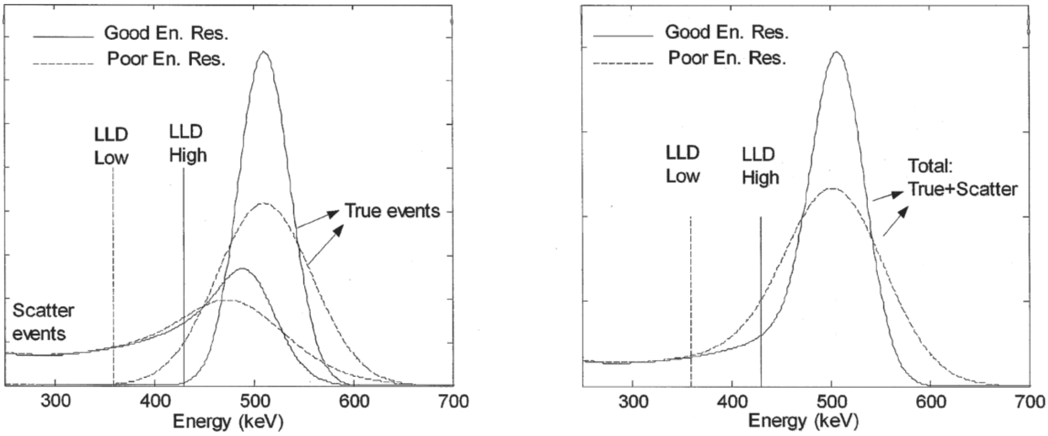

Figure 8.5. Energy spectrum for scintillators with good (solid line) and poor energy resolution (En. Res.) (dash). On the left true and scattering events are shown separated but in reality these events are indistinguishable to the detector; only the sum of the two curves is available (right). For a scintillator with good energy resolution it is possible to set the low-level discriminator (LLD) at a higher level to reject scatter with minimal loss of true events.

For the incoming photon to deposit all its energy, it is important that the photon-crystal interaction be a photoelectric rather than a Compton event. Because the likelihood of Compton scattering is proportional to the atomic number Z of the medium, whereas the likelihood of a photoelectric event is proportional to Z^5, scintillators with a high Z (or effective Z for compounds) are preferable to maximize the fraction of events with full energy deposition.

It is not possible to entirely avoid statistical fluctuations, which are also an inherent part of the detection mechanism. In fact, the number of light photons n produced by a high-energy (gamma) photon is determined in a random process. For this reason, photons having the same energy produce a varying n. Other statistical processes are involved in the conversion of photons to photoelectrons and in the multiplication of electrons inside the PMT. Because the energy of the event is measured by collecting over time (integrating) the PMT current, the final effect is an imperfect energy measurement, distributed approximately along a gaussian curve, which results in the peaks in Figure 8.5. A statistical analysis of the process shows that energy resolution, which gets worse as the gaussian becomes wider, depends mainly on the light yield of the scintillator. Table 8.2 shows the light output of different scintillators. A high light output minimizes relative fluctuations in the current and is associated with good energy resolution. Figure 8.5 also shows the case of two scintillators: one with good and one with poor energy resolution. From inspection of the peaks in the figure, good energy resolution allows a more precise measurement of the energy.

Photons that undergo Compton scattering in the patient (and thus have an energy of less than 511 keV) and deposit their full energy in the detector give the contribution shown to the left of the peaks in Figure 8.5. The measured energy of these photons is also blurred by the statistical fluctuations just described. From Figure 8.5 it is clear that scatter and true events cannot be completely separated on the basis of their measured energy. However, blurring is less pronounced when energy resolution is good, which allows a relatively better separation of true from scatter events. This observation determines the choice of the LLD of the scanner. From a scatter rejection point of view, the LLD should be as high as possible. However, when the LLD is increased, eventually true events are also discarded. Optimizing the LLD setting, then, involves optimizing a trade-off between maximum sensitivity to true events and minimum sensitivity to scatter events. The advantage of good energy resolution is that it is possible to operate with a higher LLD setting, and thus reject comparatively more scatter, before a significant number of true events is lost. For the same number of true events relatively fewer scatter events are collected, which means that image processing in scanners based on a scintillator with good energy resolution can start from better estimates of the true distribution of the radiotracer.

It is important to recognize that other factors also affect energy resolution, such as size of the scintillator, homogeneity of the light output, how the scintillators are coupled to the PMTs, and the successive pulse processing. For example, to maximize energy resolution, a long time should be allowed to collect all the PMT current (integration time). However, this is at odds with the necessity of being able to process separately the next incoming event as soon as possible, that is, to achieve high count rate capabilities, which demand that integration times be kept as short as possible. Because the integration time is mainly driven by the time interval over which light is emitted, the rate at which scintillators emit light is also an important performance parameter. Table 8.2 lists decay times for different scintillators. In this case, a small value indicates a fast scintillator and thus is a desirable property. Energy resolution, then, is related to light output, but it cannot be directly inferred from it.

The data in Table 8.2 summarize all the physical parameters important for the evaluation of different scintillators. For example, NaI(T1): sodium iodide [NaI(T1)] has higher light output (and better energy resolution) than bismuth germanate (BGO) and lutetium oxyorthosilicate (LSO), for which sensitivity is much better, with LSO being also significantly faster. BGO has a much higher attenuation coefficient than NaI(Tl), and thus higher sensitivity, but the reduced light output affects negatively its energy resolution. LSO has almost the same attenuation coefficient of BGO, and is much faster than both BGO and NaI. GSO is almost as fast as LSO and in the past has offered better energy resolution at the price of reduced sensitivity. Recent improvements in LSO crystal production have led to energy resolution similar to GSO. Slight variations to the composition of LSO have recently been tested [e.g., lutetium (yttrium) oxyorthosilicate [L(Y)SO], mixed lutetium silicates (MLSs), and lutetium pyrosilicates (LPSs)]. Most of these crystals have properties similar to LSO. It is possible that scanners based on such scintillators will be developed commercially in the near future. Commercial PET scanners based on NaI(Tl), BGO, LSO, and GSO have been deployed on the field. Scanners utilizing barium fluoride ($BaF_{2)}$ and lanthanum bromide ($LaBr_3$) are of particular interest in PET instrumentation research because their fast decay times open the possibility of time-of-flight (ToF) PET. This technique is characterized by low image noise, which compensates for the disadvantage of the relatively low sensitivity of these materials. BaF_2 was among the first scintillators considered for ToF PET; more recently, interest has been focusing on $LaBr_3$ because its timing performance is competitive with BaF_2 (8) and its superior light output and energy resolution are expected to result in improved spatial resolution and rejection of scatter events.

Light Coupling and Spatial Assignment of Events

The discussion has so far focused on the efficiency of the detection of one of the two annihilation photons and on the accuracy of the measurement of its energy. Different techniques are used to identify the position at which incoming photons are detected. A possible approach is to consider them as different compromises between two extreme designs.

In the first design, a large, continuous crystal is used and the position of the event is read as in a conventional Anger (gamma) camera. In this design, the light following an interaction is shared by several PMTs facing the crystal (Fig. 8.6A) (9,10). The position of the event is calculated by a weighted average of the coordinates of the center of each PMT, where the weights are determined by the light intensity seen by

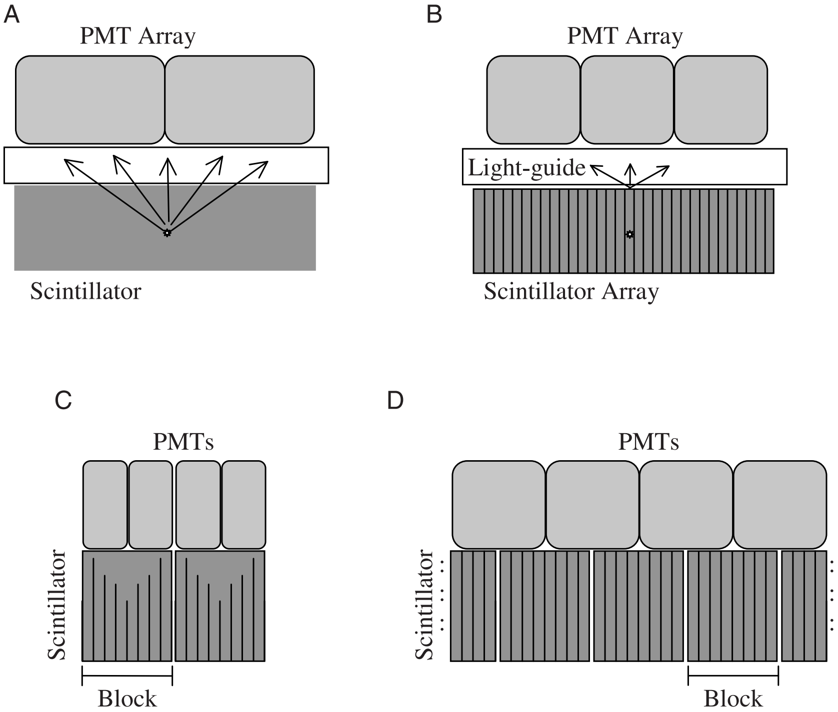

Figure 8.6. Different PET designs. A: Continuous crystal, Anger logic positioning. B: Pixelated crystal, Anger logic positioning. C: Block detectors (two shown). D: Block detectors (quadrant sharing). In designs C and D, light is allowed to spread within each block.

each PMT. This positioning strategy is often called Anger logic, after the name of its developer. For this scheme to work, light needs to spread to several PMTs to allow an accurate calculation of the position. The energy of the event is calculated from the sum of the signals from all PMTs. The same statistical fluctuations that limit energy resolution, then, affect the spatial localization of the event and thus spatial resolution. For this reason, Anger logic designs perform best with scintillators with a high light output. The typical intrinsic resolution of an Anger camera is about 3 mm in SPECT applications but is worse (~5 mm) for PET applications, due to the thicker crystals (25.4 mm NaI vs. 9.3 mm NaI) used to achieve reasonable sensitivity at the energy of the more penetrating 511-keV photons. The major disadvantage of this design is that, following each event, light invades a significant portion of the large crystal and its detection involves several PMTs. Consequently, a large area of the detector is not available for recording other events. This leads to high dead time and decreased maximum count rates.

In the second design, the scintillator is cut in an array of very small crystals (pixels), each of which is connected to a single light detector (one-to-one coupling). The advantage of a pixelated design is that the intrinsic spatial resolution of the detector is about half the size of the pixels, which can be cut to a cross section of a few millimeters. A second advantage is that, because pixels are entirely independent, count rate capabilities are much improved. Whereas the continuous crystal design has been implemented in a commercial clinical scanner, one-to-one coupling has been implemented only in small animal and brain research scanners. Its drawbacks are significantly increased cost and complexity because of the large number of small light detectors needed, as well as compromised energy resolution, especially as crystals are made smaller. Hence its application to systems that use fewer pixels and light detectors.

Most commercial clinical scanners follow neither of these designs but rather different degrees of compromise between the two extremes. A first architecture, conceptually relatively close to the continuous-crystal design, connects small, independent crystals to a light guide, which is then read out by PMTs in an Anger logic configuration (11) (Fig. 8.6B). The design of the crystals and the light guide carefully limits the number of PMTs involved in the detection of a photon; because scintillation light is not allowed to invade the whole crystal, fewer PMTs are involved and the count rate capability is improved. In the block detector architecture (12), groups of crystals (typically an 8 × 8 cluster) are connected to a 2 × 2 array of PMTs (Fig. 8.6C). The light generated in each crystal is allowed to spread in a controlled manner within the block (this is why crystals are formed by cutting slots of different depths in a block of scintillator) to only four PMTs, which, by use of Anger logic over this very limited area, can identify the crystal in which detection occurs. In yet another design, PMTs assigned to a block are replaced by larger PMTs straddling quadrants of adjacent blocks (quadrant sharing block geometry) (13).

An important parameter for comparison is the encoding ratio, which is the average number of crystals per PMT. For a given number of crystals of a given size (i.e., for comparable field of view and resolution), independently of the scintillator used, the encoding ratio is inversely proportional to the number of PMTs used. If large PMTs are used, fewer are needed to cover all crystals and the encoding ratio is large. This reduces cost; however, large PMTs also result in reduced count rate capability, because each PMT must serve a large area. Large PMTs are typically used with the continuous light guide and the continuous or pixelated crystal geometry discussed above, which have the advantage of uniform light collection over large areas. This uniformity benefits the energy resolution of the scanner. The best energy resolution is obtained in conjunction with scintillators with high light output. At the other end of the spectrum, scintillators with a low light output are best used with smaller PMTs in a block detector geometry. This has the advantage of more independent modules, which benefits the count rate, but energy resolution is sacrificed with cost and system complexity, which increase because of the larger number of PMTs needed.

Depth of Interaction

To locate accurately the annihilation photons, the scintillator in an ideal scanner would be infinitely dense and thin. To achieve workable sensitivity, real scanners must use scintillators with thickness on the order of 20 to 30 mm, which are not negligible values. Reconstruction algorithms, however, assume that photon detection takes place at the crystal surface. Figure 8.7 illustrates how this results in a degradation of spatial resolution far from the center of the scanner. The degradation increases with the thickness of the crystals as well as with the distance from the center of the scanner, where it vanishes. At 10 cm from the center, it is typically a few tenths of a millimeter. Depth of interaction, thus, is not likely to play a major role in general and especially in pediatric PET for younger patients, who are imaged only at the center of the scanner. Several schemes have been proposed to mitigate the

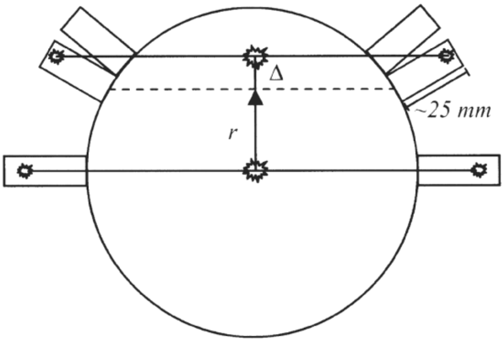

Figure 8.7. Pictorial representation of event misplacement due to depth of interaction. Due to penetration, photons can be detected well inside the crystals, but, because no information on the depth of interaction is available, reconstruction algorithms assume that detection takes place at the inside surface of the crystal. At the center of the scanner this has no consequences; however, depending on the radial position *r* and the length of the crystals, depth of interaction can result in the assignment of the event to an incorrect line of response (LOR) (i.e., to the dashed rather than the solid line).

problem [e.g. (14,15)], but to date none has yet been implemented in a commercial system.

Data Acquisition, Correction, and Image Reconstruction

When coincident photons are detected, the event is assigned to the LOR corresponding to the two detection locations and stored. The number of events detected in each LOR is the basic output of the scanner. These raw data are the starting point of image reconstruction. The scanner also acquires other data for the various corrections necessary, for example, for random events, scattering, and attenuation.

Detected events whose energy is above the energy threshold (the LLD) are often called single events. If a second single event is detected inside the time coincidence window, a prompt coincidence is obtained. This is not necessarily a true event because photons may have undergone scattering or may have originated from different nuclei ("random" event). Ideally, only true events should be used for reconstruction, but all three kinds are inevitably present in the acquired data, in varying proportions depending on the activity present in the field of view of the scanner, its distribution, and that of the scattering material, along with acquisition parameters such as the time coincidence window and the LLD setting, and the geometry of the scanner, which can be designed for 2D or fully 3D imaging.

The simplest PET scanner is composed of a single ring of detectors and thus is capable of acquiring data only in a single transverse plane, that of the ring. Extension to 3D imaging can follow different avenues. The most straightforward is to stack rings of detectors axially and, at the same time, to use tungsten septa to narrow the angle of acceptance of each ring to admit only events originating in the plane of that ring and of a few adjacent rings. In this design, rings operate independently (2D geometry). An alternative is to allow all rings to see the entire object, in which case a fully 3D geometry is realized.

Purely transverse data are sufficient for reconstruction of a 3D volume by stacking 2D transverse images, each generated independently from a 2D reconstruction of 2D data. The advantage of 3D geometry is its higher sensitivity. The elimination of the septa, however, increases the sensitivity to true as well as to random and scatter coincidences, for which the increase can be higher than for true events. Three-dimensional geometry affects scanners based on different scintillators to different degrees. In general, it places a premium on scintillators with good energy resolution (which can use a higher LLD and therefore are relatively less sensitive to scatter events) and fast timing (which are relatively less sensitive to random events and can better handle the increased count rate). It is mainly because of scatter that, in practice, in spite of the development of specific correction methods, 3D scanners based on crystals with relatively low energy resolution have not yet achieved performance consistently superior to 2D scanners, with effects measurable in terms of contrast recovery and detectability (16). This fact increases the emphasis on the scatter and random coincidence compensation methods described below.

As compared to SPECT, PET data lend themselves to correction for physical effects such as attenuation and scatter rather naturally, paving the way for quantitative imaging, that is, for the evaluation of the activity per unit volume present in the object. To reach this goal, considerable effort has been spent in the development of accurate correction methods.

Normalization

Reconstruction algorithms usually rely on the assumption of an ideal scanner, that is, one for which all parts of the detector ring are uniformly sensitive to incoming photons. In real scanners, a number of factors deviate from this assumption. Normalization is a procedure that corrects the raw data to restore the conditions of an ideal scanner with uniform sensitivity prior to reconstruction. Normalization techniques can be based on the acquisition of data on the scanner, on mathematical models, or on a combination of these two methods (17–21). Regardless of the technique used, normalization data do not need to be acquired for every study. However, because some factors, especially the calibration of the electronics, may drift over time, normalization should be part of quality control procedures and carried out periodically.

Attenuation Correction

As previously discussed, accurate attenuation correction can be achieved from knowledge of the attenuation exponentials $e^{-\mu\rho D}$ for every LOR (22–24). In the simplest methods, these are determined from the emission image by assuming that all regions containing activity have uniform attenuation. Attenuation exponentials are then determined automatically for each LOR by calculating the length of its intersection with these regions. These approaches work well for rather homogeneous parts of the body, such as in brain scans, and have the advantage of introducing no noise into image reconstruction. However, they rely on the assumption of uniform attenuation and so they are much less accurate for irregular distributions of the scatter medium, as in the chest, where the lungs present an attenuation coefficient significantly different from adjacent regions. In these situations, attenuation is better measured with a transmission scan, in which the patient is exposed to an external source of photons. In dedicated PET scanners, line sources of either germanium 68/gallium 68 (^{68}Ge/^{68}Ga) (511 keV) or cesium 137 (^{137}Cs) (662 keV) (25–27) have been used. In PET-CT scanners, it is possible to take advantage of the superior resolution and accuracy of CT data for attenuation correction. However, care must be taken in rescaling the attenuation data from the energy of the measurement (about 60 keV) to 511 keV and in considering the effects of contrast agents, if used. Another potential concern is the incorrect spatial alignment (registration) of the data, which are now effectively acquired on two different scanners, and the consistency of PET with CT data, in which the effects of the patient's breathing may be different due to the much shorter duration of the scan.

The effect of attenuation correction is usually obvious in PET images: corrected studies restore activity in the inner parts of the body to its correct, higher level. Because photons are attenuated more when more material is present, the magnitude of the correction is directly related to the size of the patient.

Random Events Subtraction

Different correction methods for random events are available. Some involve processing of the acquired data, but the most accurate approach requires that additional data with a delayed timing window also be acquired. A delayed timing window is one accepting events coming within a time τ after a time (the delay) much larger than τ has elapsed since the detection of the first event. These are the so-called delayed coincidences. In true and scatter events, the two photons identifying the LOR originate from the same nuclear decay and thus arrive at the scanner separated by a time shorter than τ. Therefore, these events are excluded from the delayed coincidences. On the other hand, random coincidences involve the decay of two different, unrelated nuclei, which happen to produce annihilation photons at the same time by chance. The method of the delayed coincidences assumes that this chance is the same as the chance of producing the photons with a time difference equal to the delay. In summary, delayed coincidences contain only random events that, although not the very same that are part of the image, are still an excellent estimate that can be subsequently subtracted from the data collected with no delay, that is, the actual scan. Whereas subtraction of noisy data from noisy data increases image noise, averaging techniques [also known as variance reduction techniques (28,29)] have been developed to minimize this problem.

The number of collected random events is proportional to the time coincidence window τ and the square of the singles count rate. Thus, their impact is less relevant in scanners based on a fast scintillator (for which τ can be set to a small value) and when low activity is present in the field of view. Because this is usually the case in pediatric PET, especially for younger patients, it is expected that the magnitude of the correction for random events will be smaller than for adults.

Scatter Correction

Accurate scattering correction is vital for accurate quantification, especially in fully 3D scanners, where the open geometry increases sensitivity to scatter events more than to true events.

In theory, because the energy of each incoming photon is available after its detection, scatter could be rejected by simply discarding all detected photons whose energy is not the 511 keV expected for an unscattered photon. In practice, because detectors do not have perfect energy resolution, scattered photons may appear as true events and vice versa. As previously discussed, a careful choice of the LLD minimizes the number of scatter events collected without unduly sacrificing sensitivity to true events. However, some scatter events are still accepted, and for a complete correction additional data processing is necessary.

Different approaches to the problem have been proposed and have evolved over the years (30–37). Most take advantage of the fact that the scatter distribution is very smooth, that is, even though it can be markedly asymmetric, it varies slowly across the field of view, and it is not very sensitive to sudden variations in the object. Recently, the steady increase in affordable computational capacity has made practical techniques that estimate the spatial distribution of scatter directly from physical principles. These are single scatter simulation (SSS) and Monte Carlo (MC) algorithms (38–40). The calculation starts from the estimate of the distribution of the activity provided by the uncorrected image and the estimate of the scattering medium provided by the attenuation scan. Application of physical laws such as Equation 7 generates an estimate of the scatter distribution, which is then subtracted from the uncorrected image to generate a more accurate estimate of the activity distribution. This estimate is still incorrect because it is still based on the uncorrected image. However, the procedure can be repeated to improve accuracy, until further repetitions do not produce significant corrections. Such techniques have the advantage of being patient-specific and equally applicable to uniform (e.g., brain) and nonuniform (e.g., chest) regions. Single scatter simulation explicitly estimates only single scatter and incorporates the effects of multiple scatter only indirectly; MC techniques can be applied to model accurately both single and multiple scatter (41–43), which can be as much as single scatter in large patients. However, at present, MC methods still need more computational resources than routinely available and in most cases do not seem to provide significant advantages over SSS. Therefore, most clinical systems use different implementations of SSS, which has proven to provide very good estimates, except perhaps for the very heaviest patients, and superior performance than previous correction techniques (40).

Because the effect of scatter is to add a rather smooth, featureless background, the effects of scatter on the image are not as evident as those of attenuation. Nevertheless, scatter correction can have a quite dramatic impact on the extraction of quantitative data, especially from cold regions, that scatter tends to “fill in.” In this case scatter correction algorithms should restore the correct, lower intensity. As for attenuation, the relative impact of scatter on image quality is directly related to the size of the patient, large patients being more affected. For this reason, the magnitude of the scatter correction is less relevant for smaller and lighter patients. Furthermore, in this population the large majority of scatter is single scatter, for an accurate estimate of which relatively simple methods such SSS are already routinely available.

Dead Time and Decay Correction

Dead time is the amount of time during data acquisition in which the scanner is not available for processing new incoming events because it is busy processing previous ones. Data are usually acquired over a given length of time (real time); in the presence of dead time the scanner will be available only for a fraction of the real time (called the live time), and, accordingly, the recorded number of events is smaller than that which would be recorded in the absence of dead time. Correction for dead time involves multiplying the acquired data by a factor that will restore this number.

Dead time increases with the count rate in the scanner. In general, correction is necessary when data acquired at different count rates need to be compared in some way. This is the case in whole-body studies, where images are formed by juxtaposing images of adjacent sections of the body, each containing a different activity (and thus affected by different dead time); in dynamic studies, because decay and redistribution of the radiotracer cause the count rate to change; and in the evaluation of quantitative measures, such as standard uptake values (SUVs), in which the number of counts is important in an absolute, not only in a relative, sense.

At low count rates, events arrive sparsely in time and it is unlikely that an event will be lost because others have just been detected, so the dead time correction is small and may not be necessary. This is the case in many pediatric studies, in which the injected dose is typically low. However, dead time correction does not present any particular disadvantages and is usually always enabled.

It is often also necessary to correct the data for the radioactive decay of the isotope. This is obtained by keeping record of the time t elapsed between some reference time (e.g., injection) and each study, and then by multiplying the acquired data by the decay factor $e^{\lambda t}$. This multiplication restores the activity of each data set to that which would have been recorded at the reference time, thus making the data comparable to those acquired at a different time.

Figure 8.8 compares the same coronal slice of the clinical study in Figure 8.9B before and after correction for attenuation, scatter, and

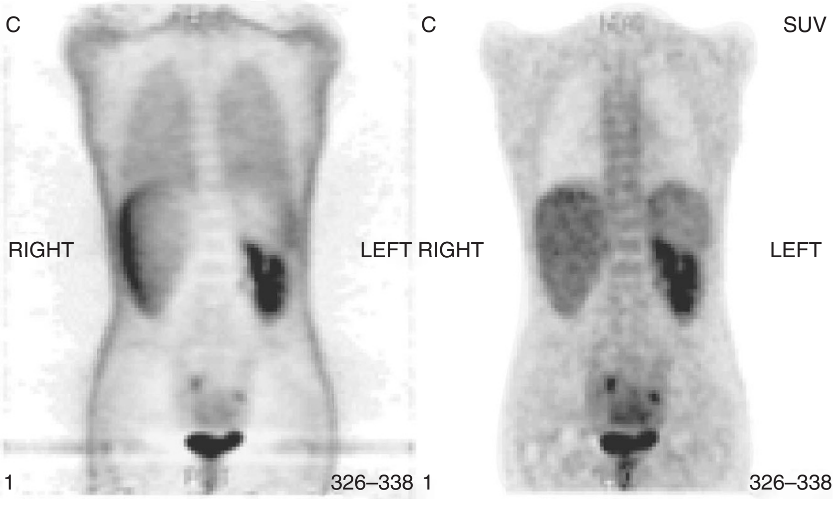

Figure 8.8. Reconstructed fluorodeoxyglucose (FDG)-PET image before (left) and after (right) correction for attenuation and scattering. Both include correction for random events, which is performed online during data acquisition.

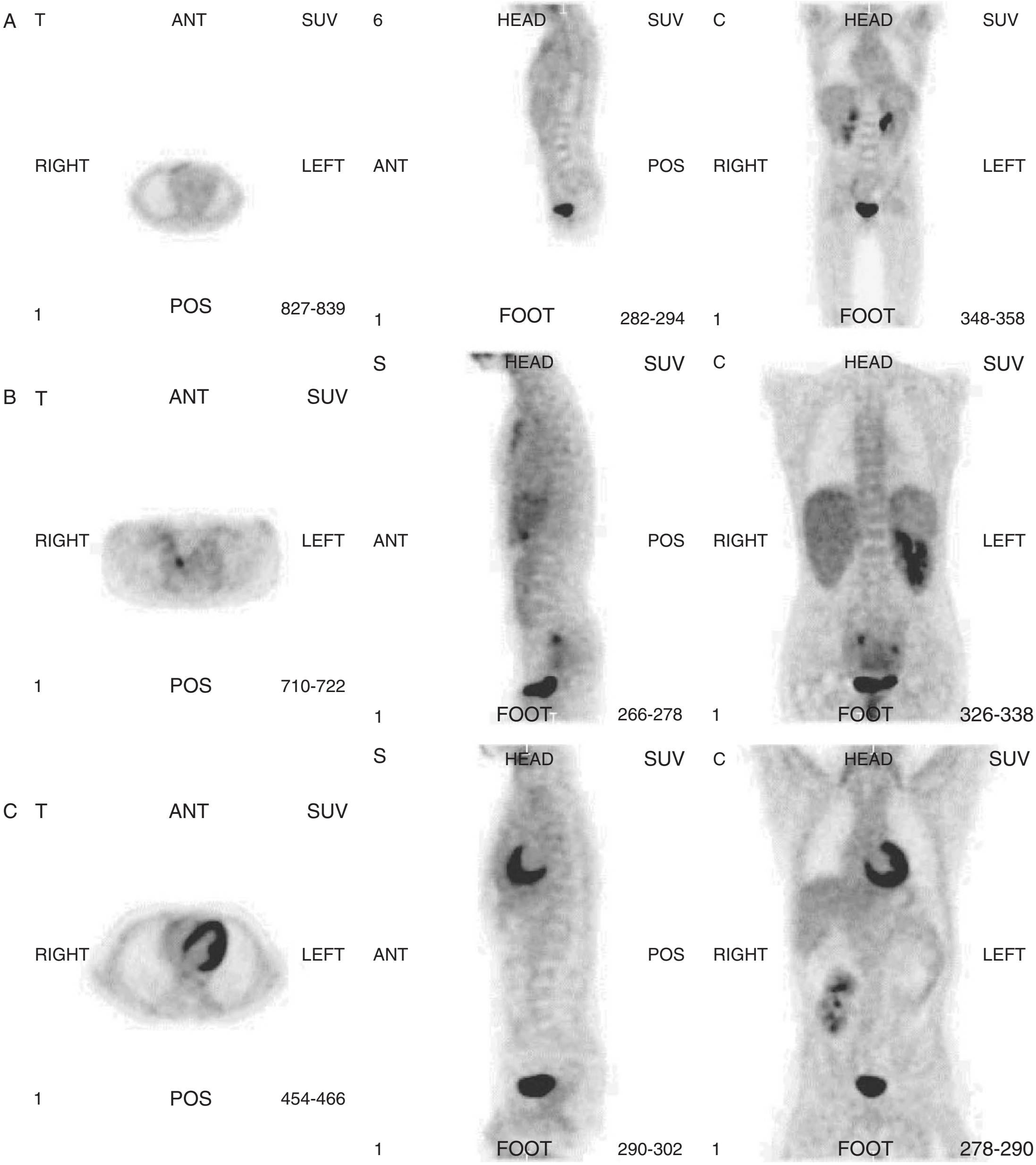

Figure 8.9. Sample whole body FDG clinical scans. A: 6-year-old girl (18 kg); B: 13-year-old girl (52.3 kg); and C: 19-year-old man (72.7 kg). Shown are representative transverse, sagittal and coronal slices.

random events. Other than the obvious artifact in slices containing the bladder, which is due to the attempt at reconstructing inconsistent data, relevant features are that before correction contrast in the lungs vs. surrounding tissue is inverted; that the sides of the body appear to have increased uptake; that the liver has not uniform uptake; and that the contrast at the site of the lesion (in the uterus) is also different from that in the corrected image.

Image Reconstruction Algorithms

A complete discussion of image reconstruction algorithms is clearly outside the scope of this overview. Only a brief summary of the most common methods used in PET imaging, with qualitative, general comments, is provided. For a more detailed overview, the interested reader is referred to the overviews offered elsewhere (44,45).

The problem of image reconstruction is to calculate the distribution of activity inside an object from the raw data. In PET, these are usually generated in the form of counts for each LOR. Most algorithms first rearrange the data in sinograms, which represent the projection of the object along a parallel, evenly spaced beam in all directions. In the 2D case, image reconstruction is similar to the reconstruction of SPECT data from a parallel-hole collimator. In every single view of the projection data, depth information has been lost, but mathematical analysis shows that if projections are taken from angles covering continuously at least 180 degrees, it is still possible to reconstruct exactly the object, slice by slice, by combining data from all directions. The image of a 3D volume is then obtained by stacking all the 2D slices. In 3D geometry, data from LORs connecting different scanner rings (i.e., for oblique tilt angles) are also acquired. The problem of fully 3D reconstruction is that these LORs cross several transverse slices; thus, it is not immediately possible to process them separately in the same way as each transverse slice.

Two different classes of algorithms are used in both 2D and 3D PET image reconstruction: analytic and iterative methods. An example of an analytic algorithm is filtered back projection (FBP), which in its 2D version is analogous to the algorithm used in other imaging modalities. Modifications of the algorithm (e.g., 3D reprojection) were introduced to handle 3D data. A common solution is the use, before reconstruction, of a rebinning algorithm to reorganize oblique into transverse data, which are then processed with 2D algorithms. The simplest approach is single-slice rebinning (SSRB) (46), which assumes that oblique data can be projected directly onto regular transverse slices, but more advanced techniques that rely on less drastic approximations, such as FOurier REbinning (FORE) (47), reduce the loss of axial resolution introduced by rebinning. The main advantage of analytic algorithms, in both 2D and 3D reconstruction, is their speed; their main drawback is that statistical noise in the data is not modeled.

Iterative algorithms handle explicitly data noise and also offer the opportunity to model more precisely the geometry of even complex scanners as well as other effects such as attenuation and scatter; however, more precise models imply much longer reconstruction times, which is the main limitation of the technique even in basic applications. Iterative algorithms start from a guess of the image and then use a computer model of the scanner and physics to predict the projection data that such guess would have generated. Comparison to the data actually acquired provides a correction factor, which is applied to the first guess to obtain a second. Iterations are continued until a satisfying image is reached. Further iteration is usually not worth the additional time and may be even harmful because excessive iteration eventually results in undesired effects such as divergence and noise amplification. Iterative algorithms differ in how updates are calculated. The most widely used method is the maximum likelihood expectation maximization (MLEM) algorithm (48,49), which estimates the object for which the probability of acquiring the data that were actually acquired is maximum. Execution can be accelerated by different variants of the algorithm, the most popular of which is ordered subset expectation maximization (OSEM) (50). Other algorithms, such as row action maximum likelihood algorithm (RAMLA) (51–53), achieve stable performance through the use of a well-chosen relaxation parameter that forces a gradual and consistent convergence toward a solution for the consistent portion of the data. Current clinical scanners implement both 2D and 3D versions of iterative algorithms. A popular solution is to use a 2D iterative algorithm, typically OSEM, in place of an analytic method after FORE. A more advanced solution is to incorporate in the iterative algorithm (e.g., RAMLA), a model of the 3D geometry. In this sense, this approach provides "fully 3D" reconstruction.

Overall, iterative algorithms are credited with better imaging performance than analytic algorithms. Their performance is particularly advantageous in whole-body studies and in low-count situations. However, especially in situations in which computational time is a limiting factor, analytic algorithms still provide a useful alternative.

Time-of-Flight Scanners

Lines of response are identified from the location of interaction of the two annihilation photons with the detector. Time-of-flight scanners are also capable of detecting the difference in the time of arrival of the two photons, from which it is possible to calculate the location of the annihilation along the LOR. In principle, this would completely locate the event in 3D, and thus altogether eliminate the need for reconstruction. Unfortunately, this is only a theoretical possibility. In fact, to locate the event along the LOR within, say, 5 mm, it would be necessary to detect a time difference of about 30 ps (30 millionths of a millionth of a second). In practice, with scintillators currently available, it is possible to identify time differences about an order of magnitude larger (i.e., about 300 ps), which corresponds to several centimeters—hardly enough to eliminate the need for image reconstruction. However, time information is still helpful. In fact, reconstruction of conventional PET data starts from the sum of events originating on the whole LOR. Therefore, noise propagation is more pronounced when LORs intersect a wide object, as, for example, in large patients. In ToF PET, this sum can be divided in the contributions due to different sections of the LOR, which provides relative containment of the propagation of statistical noise. Accordingly, all other factors being equal, the main advantage of ToF PET is in reduced image noise and the advantage is more significant for large patients. With current technology, thus, it is doubtful that

ToF PET will offer advantages in pediatric PET due to the small size of the patients.

System Performance

This section discusses very briefly some parameters of interest in the evaluation of the performance of PET scanners.

Resolution

The resolution of PET scanners can be obtained by measuring the size of the reconstructed image of a point source much smaller than the resolution of the scanner. From this definition, it is evident that a small numerical value is desirable. Modern whole-body clinical scanners have a resolution of 4 to 6 mm in the center of the field of view (FoV). Much better values, down to about 1 mm resolution, have been achieved in research scanners specifically designed for small-animal imaging (54,55). However, in clinical studies, images are typically reconstructed to reduce noise, which worsens resolution to about 10 mm.

Count Rate

The count rate is the rate at which events are acquired. In PET scanners a distinction is made between the rate at which photons are detected individually (singles rate) and the rate at which coincident events are acquired. Clearly, the two are related. In a typical scanner, the singles rate is a factor of about one thousand higher than the coincident count rate. Whereas it is an important performance parameter, the count rate includes all types of event. Because only true events are useful for image reconstruction, some other figure of merit should be used in the determination of the optimal dose.

Noise Equivalent Count Rate

The performance of a PET scanner is usually characterized with a figure of merit that, unlike the count rate, can also account for the presence of scatter and random coincidences along with true events. This is the noise equivalent count rate (NECR) (56). If T is the rate of collection of true events and R and S are, respectively, the collection rates of random and scatter events, then

$$NECR \equiv \frac{T^2}{T+S+R} \tag{8}$$

which assumes random correction with smoothing. The NECR has been shown to be proportional to the square of the signal-to-noise ratio in which signal is given by the true events and noise is the combined statistical fluctuation due to noise from all types of event.

The NECR is often plotted vs. the activity in the field of view of the scanner or its concentration in a standard phantom. These are the

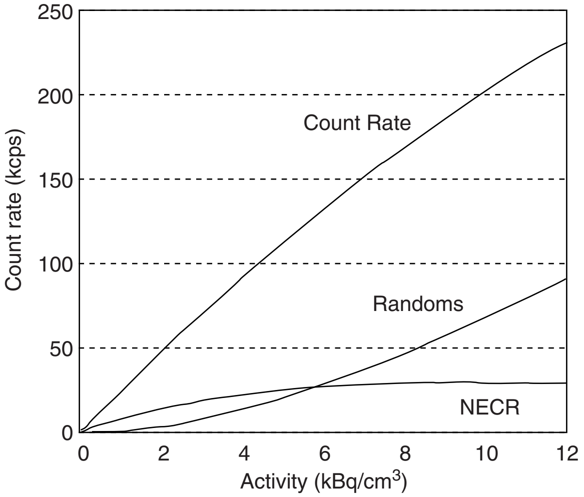

Figure 8.10. Sample noise equivalent count rate (NECR) curve of a whole-body clinical scanner (Allegro, Philips Medical Systems). The NECR is plotted vs. the activity concentration present in a 20 × 70 cm (diameter × height) phantom. Total (true + scatter + random) coincident count rate and random coincidences are also shown separately in this example. The typical dose at our institution is 5.18 kBq/cm^3 (0.14 µCi/mL).

NECR curves, an example of which is given in Figure 8.10. The NECR usually presents a maximum. The maximum is determined mainly by the rapid increase of the random count rate, also shown in Figure 8.10. Other factors being equal, desirable properties are high values of the NECR occurring at activity levels of interest in clinical practice. The activity corresponding to the maximum NECR provides an indication of the optimal operation point of the scanner. The optimal dose, however, is also determined by other factors not accounted for in the NECR curve, such as the accuracy of corrections for scatter and random events and radiation safety limits. In particular, note that once a significant fraction of the peak NECR is reached, further increase in the activity results only in progressively minor improvements in the NECR, so that the additional dose burden to the patient may not be entirely justified. For these reasons, injection doses are typically lower than the activity corresponding to the peak NECR.

These considerations show that NECR curves contain a simple, although not complete, summary of scanner performance. For this reason, NECR curves should be considered cautiously. For example, when the task is lesion detection, a better figure of merit is lesion detectability as assessed in human observer studies. Though it is possible to measure the sensitivity and specificity for the detection of lesions in PET images, these studies require data that are difficult and time-consuming to acquire, and the method of acquiring the data has not yet been standardized. For these reasons, they are not yet part of the standard protocols for the evaluation of the performance of clinical scanners.

Overview and Performance of Today's Clinical Scanners

Early PET scanners were designed as 2D systems. As solutions for the challenges of 3D imaging were developed (i.e., count rate as well as scatter and randoms correction), scanners with both 2D and 3D capability were introduced. Today, most scanners on the market operate only in 3D. This trend is also connected to the substitution of slow scintillators (mainly BGO and NaI) with significantly faster materials, such as GSO, LSO, and, more recently, LYSO, whose properties are very similar to LSO. Commercial scanners are still based on different light coupling designs, chiefly the block and the pixelated Anger detector configurations. Resolution is directly connected to the size of the crystals used, which is usually in the lower end of the range from 4 to 8 mm. Typical axial FOVs range from 15 to 18 cm. Most scanners currently sold today are sold as PET/CT units.

The fluorodeoxyglucose (FDG) scans in Figure 8.9 were acquired on one (Allegro, Philips Medical Systems Cleveland, Ohio) of the whole-body scanners currently installed at the PET center of the University of Pennsylvania. Figure 8.9A shows a 6-year-old girl (18 kg) with a history of neuroblastoma. The image shows no definite evidence of active neoplastic process. The FDG uptake is diffusely increased in the bone marrow due to the administration of colony-stimulating factors, with the exception of the midthoracic to the upper lumbar spine, where uptake is decreased, likely due to radiation therapy. Figure 8.9B shows a 13-year-old girl (52.3 kg) evaluated for possible lymphoma. The image shows two small foci of increased FDG activity in the superolateral aspect of the uterus bilaterally of uncertain etiology. Figure 8.9C shows a 19-year-old man (72.7 kg) with a history of Hodgkin's disease and a right kidney transplant. Increased uptake in the neck is likely a normal variant of muscle uptake due to contraction. Also, the transplanted kidney is visualized. The rest of the FDG distribution is normal. The absence of focal areas of abnormal FDG uptake suggests the absence of active neoplastic disease. Unattenuated 511-keV photon pairs from the center of the body vary from 20% of all events for the first patient to a little less than 10% in the heaviest. The fraction of scatter events increases with the weight of the patient from about 25% to about 35% for these three patients.

Physics Considerations in Small-Patient Imaging

The diseases to which PET has been applied for diagnosis and evaluation in adults are infrequent in pediatrics. Nevertheless, in certain applications, pediatric PET is taking up a more important role, specifically in brain imaging (epilepsy) as well as in whole-body imaging (bone tumors, lymphoma, neuroblastoma) (57). To date, no special scanners have been expressly designed for pediatric imaging; only adult scanners are used.

The pediatric population covers the range of patient sizes from newborns to young adults. Though the same considerations that apply to adults apply to children, imaging of small patients offers advantages and poses challenges for the optimal use of the instrumentation. The most obvious advantage is that in a small patient attenuation and scatter are relatively low. Also, the 3D mode should be particularly competitive for quantitative accuracy because the magnitude of the scatter compensation necessary is relatively lower. Sensitivity is particularly important to keep dose and scan time at a minimum, which may be particularly desirable in this population. On the other hand, energy resolution may be less of a concern because of the reduced need for scatter rejection. Finally, fast timing may not be necessary because of the low activity. Therefore, scanners based on high-sensitivity scintillators may be attractive in pediatrics in spite of their energy and timing resolution.

As for the overall geometry of the scanner, a smaller transverse field of view may be sufficient, especially for newborns and infants. Dedicated brain and small animal scanners were developed to take advantage of similar opportunities. It makes sense, then, to accommodate a patient sufficiently small in a brain scanner, which is designed to provide better resolution and higher sensitivity over a smaller and longer field of view than a whole-body scanner. This solution may be practical only for very few patients, likely not enough to justify the acquisition of a special purpose scanner at most institutions.

Conclusion

In pediatric PET imaging, the same scanners designed for adult imaging are used successfully. In general, PET image quality depends on the weight of the patient for a given scan time. In lighter patients, attenuation and scatter are minimized, which results in improved image quality. This is often the case in pediatric imaging, especially for younger patients. Alternatively, the improvement in image quality can be traded off for reduced scan time at constant image quality. The main challenge, in particular for the smallest patients, comes from the need for improved resolution and sensitivity, especially when lower tracer concentrations are used to minimize the dose burden to a young population. These needs can be answered with a scanner design with prolonged axial and reduced transverse field of view (and patient port). The result would then be a design similar to the adult brain scanners present at some research institutions. Operation in 3D mode seems particularly appealing again because of the low scatter and random fractions expected in pediatric studies. For the same reason, especially if low levels of activity are preferred for radiation exposure considerations, scintillators with high stopping power may be very competitive compared to less efficient or faster materials, even at the cost of relatively poor energy resolution and timing properties.

References

1. Valk PE, Bailey DL, Townsend DW, Maisey MN. Positron Emission Tomography: Basic Science and Clinical Practice. New York: Springer-Verlag, 2003.

2. Bendriem B, Townsend DW. The Theory and Practice of 3D PET. New York: Kluwer Academic Publishers, 1998.
3. Krane KS. Introductory Nuclear Physics. New York: Wiley, 1987.
4. Harpen MD. Positronium: review of symmetry, conserved quantities and decay for the radiological physicist. Med Phys 2004;31:57–61.
5. De Beneditti S, Cowan CE, Konneker WR, et al. On the angular distribution of two-photon annihilation radiation. Phys Rev 1950;77:205–212.
6. Levin CS, Hoffman EJ. Calculation of positron range and its effect on the fundamental limit of positron emission tomography system spatial resolution. Phys Med Biol 1999;44:781–799.
7. Evans RD. The Atomic Nucleus. New York: McGraw-Hill, 1955.
8. Surti S, Karp JS, Muehllehner G. Image quality assessment of LaBr3-based whole-body 3D PET scanners: a Monte Carlo evaluation. Phys Med Biol 2004;49:4593–4610.
9. Karp JS, Muehllehner G, Mankoff DA, et al. Continuous-slice PENN-PET: a positron tomograph with volume imaging capability. J Nucl Med 1990;31: 617–627.
10. Adam LE, Karp JS, Daube-Witherspoon ME, Smith RJ. Performance of a whole-body PET scanner using curve-plate NaI(Tl) detectors. J Nucl Med 2001;42:1821–1830.
11. Surti S, Karp JS, Freifelder R, Liu F. Optimizing the performance of a PET detector using discrete GSO crystals on a continuous lightguide. IEEE Trans Nucl Sci 2000;47:1030–1036.
12. Nutt R, Casey M, Carroll LR, Dahlbom M, Hoffman EJ. A new multi-crystal two-dimensional detector block for PET. J Nucl Med 1985;26:P28.
13. Wong WH, Uribe J, Hicks K, Hu GJ. An analog decoding BGO block detector using circular photomultipliers. IEEE T Nucl Sci 1995;42:1095–1101.
14. Moses WW, Derenzo SE. Design studies for a PET detector module using a pin photodiode to measure depth of interaction. IEEE Trans Nucl Sci 1994;41:1441–1445.
15. Casey ME, Eriksson L, Schmand M, et al. Investigation of LSO crystals for high spatial resolution positron emission tomography. IEEE Trans Nucl Sci 1997;44:1109–1113.
16. El Fakhri G, Holdsworth C, Badawi RD, et al. Impact of acquisition geometry and patient habitus on lesion detectability in whole-body FDG-PET: a channelized Hotelling observer study. Presented at IEEE Nuclear Science Symposium and Medical Imaging Conference, Norfolk, VA, 2002.
17. Defrise M, Townsend DW, Bailey D, Geissbuhler A, Michel C, Jones T. A normalization technique for 3D PET data. Phys Med Biol 1991;36:939–952.
18. Bailey DL, Townsend DW, Kinahan PE, Grootoonk S, Jones T. An investigation of factors affecting detector and geometric correction in normalization of 3–D PET data. IEEE Trans Nucl Sci 1996;43:3300–3307.
19. Badawi RD, Lodge MA, Marsden PK. Algorithms for calculating detector efficiency normalization coefficients for true coincidences in 3D PET, Phys Med Biol 1998;43:189–205.
20. Badawi RD, Marsden PK. Developments in component-based normalization for 3D PET. Phys Med Biol 1999;44:571–594.
21. Badawi RD, Ferreira NC, Kohlmyer SG, Dahlbom M, Marsden PK, Lewellen TK. A comparison of normalization effects on three whole-body cylindrical 3D PET systems. Phys Med Biol 2000;45:3253–3266.
22. Carroll LR, Kertz P, Orcut G. The orbiting rod source: improving performance in PET transmission correction scans. In: Esser PD, ed. Emission Computed Tomography: Current Trends. Society of Nuclear Medicine, New York, 1983.

23. Huesman RH, Derenzo SE, Cahoon JL, et al. Orbiting transmission source for positron tomography. IEEE Trans Nucl Sci 1988;35:735–739.
24. Daube-Witherspoon M, Carson RE, Green MV. Postinjection transmission attenuation measurements for PET. IEEE Trans Nucl Sci 1988;NS-35:757–761.
25. deKemp RA, Nahmias C. Attenuation correction in PET using single photon transmission measurement. Med Phys 1994;21:771–778.
26. Karp JS, Muehllehner G, Qu H, Yan XH. Single transmission in volume-imaging PET with a Cs-137 source. Phys Med Biol 1995;40:929–944.
27. Smith RJ, Karp JS. Post-injection transmission scans in a PET camera operating without septa with simultaneous measurement of emission activity contamination. IEEE Trans Nucl Sci 1996;43:2207–2212.
28. Casey ME, Hoffman EJ. Quantitation in positron emission computed-tomography. 7. A technique to reduce noise in accidental coincidence measurements and coincidence efficiency calibration. J Comput Assist Tomogr 1986;10:845–850.
29. Badawi RD, Miller MP, Bailey DL, Marsden PK. Random variance reduction in 3D PET. Phys Med Biol 1999;44:941–954.
30. Karp JS, Muehllehner G, Mankoff DA, et al. Continuous-slice PENN-PET—a positron tomograph with volume imaging capability. J Nucl Med 1990; 31:617–627.
31. Cherry SR, Huang SC. Effects of scatter on model parameter estimates in 3D PET studies of the human brain. IEEE Trans Nucl Sci 1995;42:1174–1179.
32. Bergstrom M, Martin W, Pate B. A look at anatomical and physiological brain images. Dimensions Health Serv 1983;60:36.
33. Hoverath H, Kuebler WK, Ostertag HJ, et al. Scatter correction in the transaxial slices of a whole-body positron emission tomograph. Phys Med Biol 1993;38:717–728.
34. Bailey DL, Meikle SR. A convolution-subtraction scatter correction method for 3D PET. Phys Med Biol 1994;39:411–424.
35. Bendriem B, Trebossen R, Frouin V, Syrota A. A PET scatter correction using simultaneous acquisitions with low and high lower energy thresholds. Presented at 1993 IEEE Nuclear Science Symposium and Medical Imaging Conference, San Francisco, CA, 1993.
36. Grootoonk S, Spinks TJ, Sashin D, Spyrou NM, Jones T. Correction for scatter in 3D brain PET using a dual energy window method. Phys Med Biol 1996;41:2757–2774.
37. Adam LE, Karp JA, Freifelder R. Energy-based scatter correction for 3–D PET scanners using NaI(Tl) detectors. IEEE Trans Med Imaging 2000;19: 513–521.
38. Ollinger JM. Model-based scatter correction for fully 3D PET. Phys Med Biol 1996;41:153–176.
39. Watson CC, Newport D, Casey ME, deKemp RA, Beanlands RS, Schmand M. Evaluation of simulation-based scatter correction for 3-D PET cardiac imaging. IEEE Trans Nucl Sci 1997;44:90–97.
40. Accorsi R, Adam LE, Werner ME, Karp JS. Optimization of a fully 3D single scatter simulation algorithm for 3D PET. Phys Med Biol 2004;49: 2577–2598.
41. Levin CS, Dahlbom M, Hoffman EJ. A Monte-Carlo correction for the effect of Compton-scattering in 3-D PET brain imaging. IEEE Trans Nucl Sci 1995;42:1181–1185.
42. Holdsworth CH, Levin CS, Farquhar TH, Dahlbom M, Hoffman EJ. Investigation of accelerated Monte Carlo techniques for PET simulation and 3D PET scatter correction. IEEE Trans Nucl Sci 2001;48:74–81.

43. Holdsworth CH, Levin CS, Janecek M, Dahlbom M, Hoffman EJ. Performance analysis of an improved 3-D PET Monte Carlo simulation and scatter correction. IEEE Trans Nucl Sci 2002;49:83–89.
44. Lewitt RM, Matej S. Overview of methods for image reconstruction from projections in emission computed tomography. Proc IEEE 2003;91:1588–1611.
45. Defrise M, Kinahan PE, Michel C. Image reconstruction algorithms in PET. In: Valk PE, Bailey D, Townsend DW, Maisey MN, eds. Positron Emission Tomography: Basic Science and Clinical Practice. New York: Springer-Verlag, 2003:91–114.
46. Daube-Witherspoon ME, Muehllehner G. Treatment of axial data in three-dimensional PET. J Nucl Med 1987;28:1717–1724.
47. Defrise M, Kinahan PE, Townsend DW, Michel C, Sibomana M, Newport DF. Exact and approximate rebinning algorithms for 3D PET data. IEEE Trans Med Imaging 1997;11:145–158.
48. Shepp L, Vardi Y. Maximum likelihood reconstruction for emission tomography. IEEE Trans Med Imaging 1982;MI-1:113–122.
49. Lange K, Carson R. EM reconstruction algorithms for emission and transmission tomography. J Comput Assist Tomogr 1984;8:306–316.
50. Hudson HM, Larkin RS. Accelerated image reconstruction using ordered subsets of projection data. IEEE Trans Med Imaging 1994;13:601–609.
51. DePierro AR. On some nonlinear iterative relaxation methods in remote sensing. Matematica Aplicada Computacional 1989;8:153–166.
52. Browne JA, DePierro AR. A row-action alternative to the EM algorithm for maximizing likelihoods in emission tomography. IEEE Trans Med Imaging 1996;15:687–699.
53. Daube-Witherspoon ME, Matej S, Karp JS. Assessment of image quality with a fast fully 3D reconstruction algorithm. In: Siebert JA, ed. 2001 IEEE Nuclear Science Symposium and Medical Imaging Conference. Piscataway, NJ: Institute of Electrical and Electronics Engineers, 2002:M14–12.
54. Jeavons AP, Chandler RA, Dettmar CAR. A 3D HIDAC-PET camera with sub-millimetre resolution for imaging small animals. IEEE Trans Nucl Sci 1999;46:468–473.
55. Tai YC, Chatziioannou AF, Yang YF, et al. MicroPET II: design, development and initial performance of an improved microPET scanner for small-animal imaging. Phys Med Biol 2003;48:1519–1537.
56. Strother SC, Casey ME, Hoffman EJ. Measuring PET scanner sensitivity—relating count rates to image signal-to-noise ratios using noise equivalent counts. IEEE Trans Nucl Sci 1990;37:783–788.
57. Jadvar H, Connolly LP, Shulkin BL. PET imaging in pediatric disorders. In: Valk PE, Bailey D, Townsend DW, Maisey MN, eds. Positron Emission Tomography: Basic Science and Clinical Practice. New York: Springer-Verlag, 2003:755–774.